Iodine chemistry determines the defect tolerance of lead-halide perovskites

Daniele Meggiolaro,[a,b] Silvia G. Motti,[c,d] Edoardo Mosconi,[a,b] Alex J. Barker,[c] James Ball,[c] Carlo Perini,[c] Felix Deschler,[e] Annamaria Petrozza,[c] Filippo De Angelis [a,b]

[a]Computational Laboratory for Hybrid/Organic Photovoltaics (CLHYO), CNR-ISTM, Via Elce di Sotto 8, 06123, Perugia, Italy.

[b]CompuNet, Istituto Italiano di Tecnologia, Via Morego 30, 16163 Genova, Italy.

[c] Center for Nano Science and Technology @Polimi, Istituto Italiano di Tecnologia, via Giovanni Pascoli 70/3, 20133, Milan, Italy.

[d]Dipartimento di Fisica, Politecnico di Milano, Piazza Leonardo da Vinci, 32, 20133 Milano, Italy.

[e]Cavendish Laboratory, University of Cambridge, JJ Thomson Avenue, Cambridge, CB3 0HE, UK

Table of Contents graphics

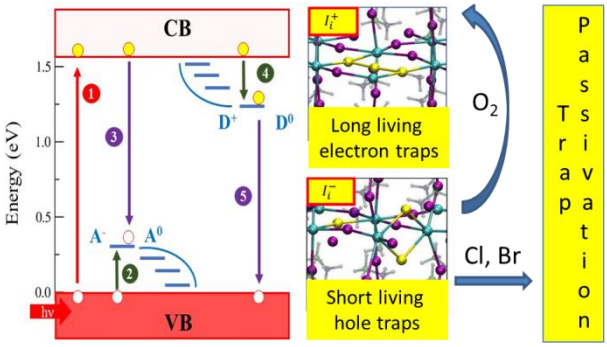

Electron/hole traps related to positive/negative interstitial iodine dominate the defect chemistry of $MAPbI_3$, related to the typical iodine redox chemistry.

Abstract

Metal-halide perovskites are outstanding materials for photovoltaics. Their long carrier lifetimes and diffusion lengths favor efficient charge collection, leading to efficiencies competing with established photovoltaics. These observations suggest an apparently low density of traps in the prototype methylammonium lead iodide ($MAPbI_3$) contrary to the expected high defect density of a low-temperature, solution-processed material. Combining first-principles calculations and spectroscopic measurements we identify less abundant iodine defects as the source of photochemically active deep electron and hole traps in $MAPbI_3$. The peculiar iodine redox chemistry leads, however, to kinetic deactivation of filled electron traps, leaving only short-lived hole traps as potentially harmful defects. Under mild oxidizing conditions the amphoteric hole traps can be converted into kinetically inactive electron traps, providing a rationale for the defect tolerance of metal-halide perovskites. Bromine and chlorine doping of $MAPbI_3$also inactivate hole traps, possibly explaining the superior optoelectronic properties of mixed-halide perovskites.

Methylammonium lead iodide ($MAPbI_3$, $MA=CH_3NH_3^+$) and related metal-halide perovskites are outstanding materials for photovoltaics.[1] Strong light absorption and low exciton binding energy[2-4] coupled to the low recombination rate of photogenerated charge carriers are the primary reasons for the incredible success of this class of materials.[5] The long carrier lifetimes and diffusion lengths[6] favors efficient charge collection at selective contacts, leading to power conversion efficiencies competing with established thin film photovoltaics.[7, 8] Together with the screening of charge carriers due to the possible formation of polarons,[9-11] these observations suggest an apparently low density of traps in $MAPbI_3$, contrary to the expected high defect density of a low-temperature, solution-processed material. Very low trap densities of $\sim 10^{11}$ cm^{-3} have indeed been reported for $MAPbI_3$ single crystals,[12,13] which increase up to $\sim 10^{16}$ cm^{-3} for polycrystalline thin films used in efficient solar cells.[13-15] The high trap density should dramatically affect the photovoltaic efficiency, suggesting that $MAPbI_3$ is inherently defect tolerant due to dominant defects introducing only shallow traps in the material band gap.[16-19]

The device effectiveness of metal-halide perovskites, as of any semiconductor, is intimately related to the stability and defect properties of the material, along with the aforementioned polaron-protected transport properties. Vacancies, interstitials [20] or antisites with associated ionization levels within the material band gap have a detrimental effect on solar cell performance, due to trapping of photogenerated carriers limiting the cell voltage.[21] According to the classic Shockley-Read-Hall theory[21] the capture rate of an electron (hole) on a donor (acceptor) site is proportional to the defect densities, the free-carrier density and the carrier capture cross sections (Supplementary Information Eq. 1). Trap states with levels placed in the middle of the band gap are the most active recombination centers, with possibly dramatic effects on the solar cell efficiency.

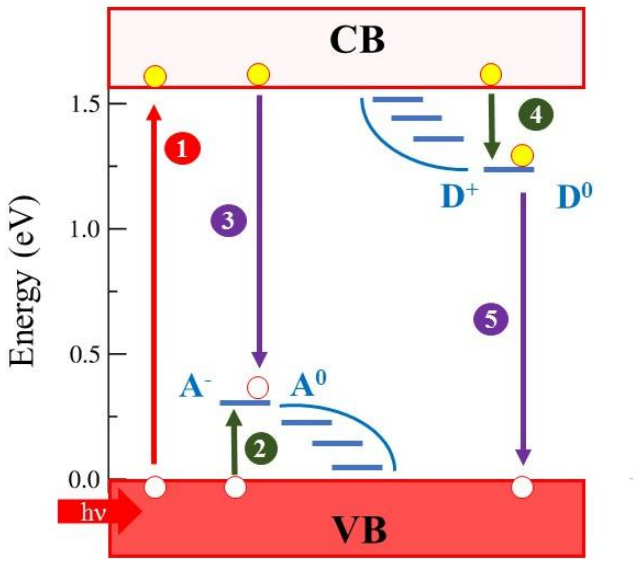

Scheme 1. Dynamics of charge trapping and recombination in $MAPbI_3$.Trap states show a distribution, ~0.2-0.3 eV above the valence band (VB) and below the conduction band (CB).[12]The relevant processes schematically reported are: 1) Above band gap photoexcitation, producing electron (yellow circles) /hole (white circles) pairs. 2), 4) Electrons (holes) are trapped in a donor (acceptor) levels. 3) , 5) Recombination (radiative or non-radiative) occurs between trapped electrons (holes) and VB holes (CB electrons).[14]

Native defects are natural products of the crystal growth and despite the use of sophisticated techniques for controlled growth conditions they are almost unavoidable. Conventional semiconductors show low to moderate trap densities (defined as the number of traps per cm^3): single crystal Si (10^8 cm^{-3}),[22] polycrystalline Si (10^{13}-10^{14} cm^{-3}),[23] CdTe (10^{13}-10^{15} cm^{-3}),[24] CIGS (10^{13} cm^{-3}).[25] Adinolfi et al.[12] showed the existence of a distribution of traps in single crystalline $MAPbI_3$, spanning 0.2-0.3 eV above and below the valence band (VB) and conduction band (CB), respectively, Scheme 1. Very low trap densities of ~10^{11} cm^{-3} have been reported, with a general consensus among different works.[13] Higher trap densities of ~10^{15}-10^{16} cm^{-3} have been reported for (large grain) polycrystalline $MAPbI_3$ thin films used in solar cell fabrication.[13-15, 26] Despite this

fairly high trap density, the efficiency of the associated solar cells are surprisingly not dramatically affected.[14, 27] Several first-principles investigations have been carried out on the nature of defects in $MAPbI_3$.[16-19, 28] The message conveyed by these studies is that native defects would introduce only shallow states in the perovskite band gap,[12] with the formation of Schottky complexes possibly leading to self-compensation effects.[19] High level calculations based on hybrid Density Functional Theory (DFT) including spin-orbit coupling have however shown that iodine interstitials induce deep levels in the $MAPbI_3$ gap,[20] which should strongly affect the solar cell performance.

Despite previous efforts, the nature, density and activity of trap states in metal halide perovskites and the reasons underlying the apparently minimal defect impact on the recombination of photogenerated carriers have remained elusive. By combining state of the art first-principles calculations with highly sensitive photoluminescence and transient absorption measurements we show here that despite the fairly high defect density due to Pb- and MA-related defects, less abundant iodine defects introduce deep electron and hole traps in $MAPbI_3$. The peculiar iodine redox chemistry leads, however, to kinetic deactivation of filled electron traps, leaving only short-lived hole traps as potentially harmful defects. The amphoteric nature of iodine traps suggests that under mild oxidizing conditions, likely met during perovskite solution synthesis, hole traps can be converted into kinetically inactive electron traps, providing a rationale for the surprising defect tolerance of metal-halide perovskites. Based on this model, we also show how bromine and chlorine doping in $MAPbI_3$ may effectively inactivate iodine hole traps, explaining the superior optoelectronic properties of mixed halide perovskites.

Results and Discussion

To quantitatively estimate the nature and density of traps in $MAPbI_3$, we investigate native defects in $MAPbI_3$ combining fairly large supercell calculations, based on hybrid DFT, including dispersion corrections and spin-orbit coupling (SOC). These ingredients are critical to obtain an accurate description of the band edges energetics,[20] as demonstrated in Supplementary Figures S1-3, and, as

we show here, of the defect formation energies (DFE), see Supplementary Tables S1-S2. We use the modified HSE06 exchange-correlation functional including 43% exact exchange proposed in Ref. [20], which, coupled to SOC, provides similar band-edge energetics to high-level GW-SOC calculations,[29] ensuring a comparable degree of accuracy. The use of DFT functionals including non-local exchange is known to be important to accurately estimate the DFE of defects characterized by unpaired electrons,[30, 31] such as the neutral I_i^0 and V_I^0 defects investigated here.

The DFEs are conventionally calculated by eq. (1):

$$DFE(X^q) = E(X^q) - E(perf) - \sum_i n_i\mu_i + q(E_F + V + \Delta V) + E^q(corr) \quad (1)$$

where $E(X^q)$ is the energy of the X defect of charge q-containing system, $E(perf)$ the energy of the perfect, non defective system, n and μ are, respectively, the number and the chemical potentials of the species added or subtracted to the non defective system to form a defect; q is the charge of the defect. The first three terms thus define the chemical energy required to form a defect from the constituting materials. As an example, for an iodine vacancy the first three terms define the energy required to break the Pb-I bond from the perfect crystal, thus creating a vacancy, and to release an iodine atom as ½ I_2. The last two terms of eq. (1), $q(E_F+V+\Delta V)$ and $E^q(corr)$, instead represents the energy associated to the exchange of electrons with the Fermi level of the system, corrected for the electrostatic potential shift ΔV of the defective system induced by the defect charge and the long range electrostatic interaction between the periodic defects images. The Fermi level is allowed to vary within the band gap and is referenced to the valence band maximum (VBM) of the pristine crystal, i.e. E_F=0 at the top of the valence band. Following eq. 1, the defect formation energy of a charged defect varies linearly as the Fermi energy scans the material band gap, with a slope fixed by the charge state q of the defect. Different charge states of the same defect can thus have different DFEs, and the intersection point between the DFEs lines of various charge states define the point at which a certain defect will change its charge state, thus the defect ability to trap or release electrons. These intersection points are called thermodynamic ionization levels, effectively corresponding to

oxidation and reduction potentials of the defective system, and their position with respect to the band edges defines whether a defect will act as a (shallow or deep) trap for photogenerated charge carriers, with ionization levels within the band gap, or not. Knowledge of the DFEs allows one to calculate the defect density by a Boltzmann statistics and the native Fermi level by searching for the condition of electroneutrality of the system, see Methods for further details.

The DFE diagram of $MAPbI_3$ grown in stoichiometric conditions, corresponding to 1:1 ratio of the PbI_2 and MAI precursors, and the associated thermodynamic ionization levels are reported in Figures 1a and 1b, see Supplementary Figure S3 for iodine-rich and iodine-poor conditions. In iodine-medium conditions the most stable defects, *i.e.* those with the lowest DFEs, are MA interstitials (MA_i^+), interstitial iodine (I_i) and lead vacancies (V_{Pb}^{2-}) which pin the Fermi level roughly at mid-gap (~0.7 eV above the VB over a 1.58 eV calculated band gap), as shown in Figure 1a. Notice the different slope of the DFE variation with the Fermi energy for the differently charged defects, *e.g.* MA_i^+ and V_{Pb}^{2-}, whose DFE increases and decreases, respectively, by increasing the Fermi energy, Figure 1a. The calculated close to mid-gap native Fermi level is consistent with the intrinsic (or mildly p-doped) nature of single crystalline $MAPbI_3$,[32] while thin films probed near the surface show clear n-doping related to a Pb-rich environment.[33] Beside these more stable defects, iodine vacancy (V_I^+) and interstitial lead (Pb_i^{2+}) are found at ~0.2 eV higher DFE at the native Fermi level. Still at higher DFE we calculate MA vacancy (V_{MA}^-) and iodine/MA antisite (I_{MA}^0), see Supplementary Table S3 for a summary of DFEs and calculated defect densities. Though all defects contribute to determine the native Fermi level, their effect exponentially decreases as their DFE increases, so that the more stable MA_i^{+-}, I_i and V_{Pb}^{2-} defects mainly determine the native Fermi level. Defects mobility should also be considered to quantify the defect activity, since thermodynamically favorable defect formation can be hindered by possible high activation barriers to defect migration. Defects related to I and MA ions are the major migrating species,[34-36] with a general consensus in I being faster than MA being faster than Pb migration.[37]

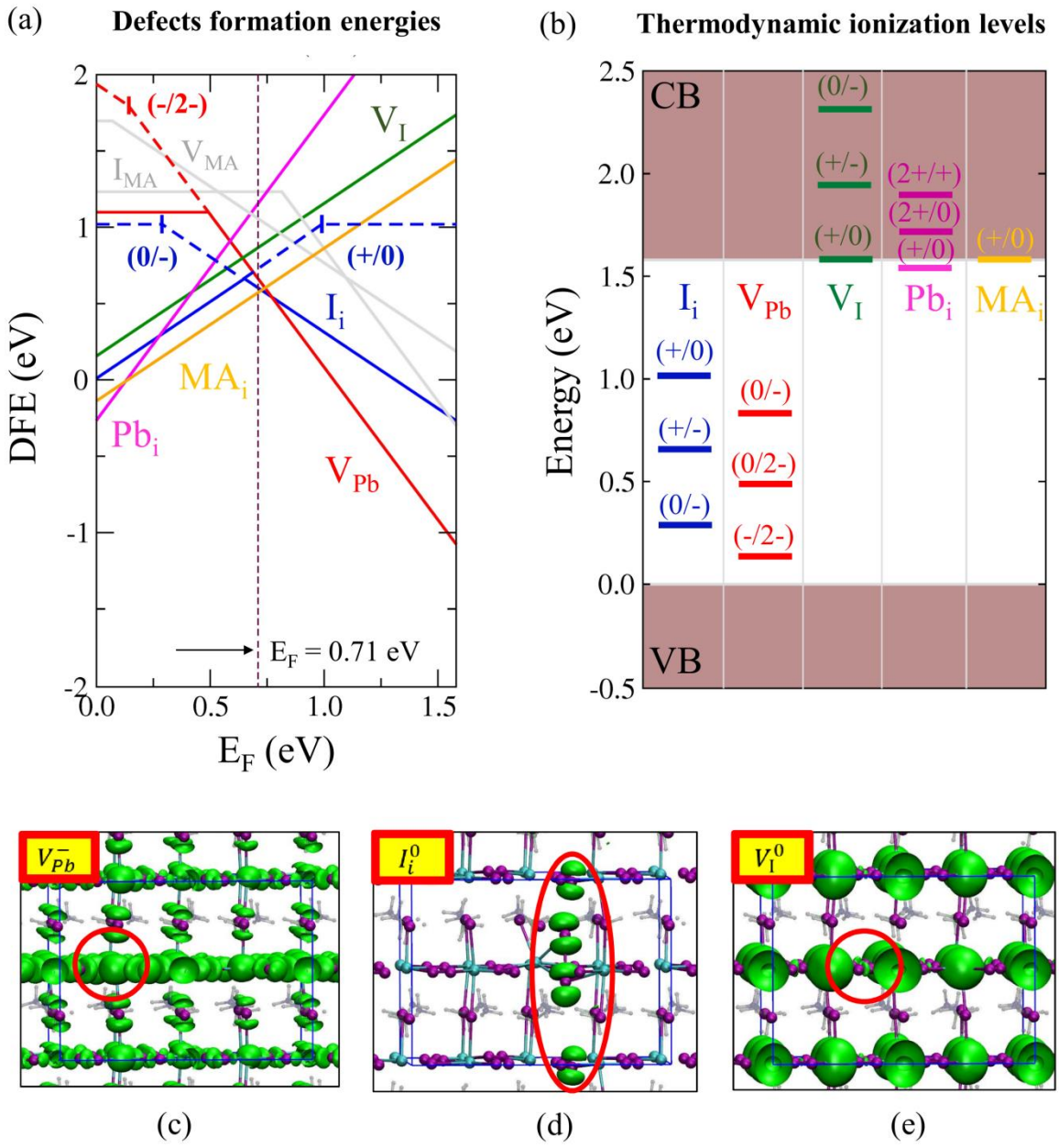

Figure 1. a) Defect formation energy (DFE, eV) diagram versus the Fermi energy (E_F, eV) for $MAPbI_3$ showing the most stable defects in stoichiometric (iodine-medium) conditions. Solid lines indicate the stable charge states of a given defect, while the blue dashed lines indicate the metastable neutral state of I_i. The energy of positive (negative) defects increases (decreases) by increasing E_F while that of neutral defects is stable with respect to E_F. E_F ranges from the top of the valence band (E_F=0) to the bottom of the conduction band E_F=1.58 eV, corresponding to the calculated band gap. The native Fermi level is indicated by the vertical black dashed line at 0.65 eV.

b) Thermodynamic ionization levels for the most stable defects calculated in a) referenced to the VB corresponding to E_F=0. The ionization levels are determined by the crossing of the lines representing different charge states of a given defect in a). c) Lowest unoccupied level of V_{Pb}^{-}, resembling delocalized VB states. d) Lowest unoccupied state of I_i^0, showing the formation of a localized state. e) Highest occupied level of V_I^0, resembling delocalized CB states.

The associated defect density is fairly high, spanning ~10^{11}-10^{12} cm^{-3} (see Supplementary Table S3) closely matching the experimental trap density measured in $MAPbI_3$ single crystals.[12]

Figure 1b shows that among the more stable defects, i.e. those with fairly low DFE, only V_{Pb} and I_i exhibit charge transitions within the $MAPbI_3$ band gap. Due to the interplay of the various terms of eq. (1) in determining the thermodynamic ionization levels, our HSE06-SOC results show significant differences compared to previous studies[28] and to our PBE data, see Supporting Figure S2, which predict a shallow trapping activity for I_i, V_{Pb} and MA_i and deep trapping for Pb_i. As previously noted,[20] V_I^+ has a transition level resonant with the CB, thus although showing a low activation energy to migration,[38] it can at most represent a shallow trapping site in bulk crystals. The shallow nature of V_I^+ is confirmed also in the presence of dynamic fluctuations, despite the vacancy motion is coupled to that of the MA cations.[39]

At the calculated native Fermi level V_{Pb} is stable in the 2- charge state, thus this defect could trap holes by the -/2- transition level whose energy falls 0.13 eV above the VB, suggesting a shallow trapping activity. The 0/2- transition implies the trapping of two holes on the same defect site, and as such it has a vanishingly small capture cross section. The 0/- transition is not active due to the instability of V_{Pb}^0 at the native Fermi level, implying a negligible density of the neutral charge state. Furthermore, the activation energy associated to V_{Pb}^{2-} defect migration (~1 eV or higher) suggests that the nucleation of metallic Pb is likely to occur at the surface of the crystal only at high temperatures or under high energy irradiation.[33]

While shallow traps, lying ~ 25 meV below the CB, were found in large-grain $MAPbI_3$ thin films in previous studies,[24] here we conclude that interstitial iodine is likely the only stable and active trap source among native point defects.[20] Lending support to the predicted defect chemistry, recent X-ray and neutron diffraction measurements on $MAPbI_3$ revealed significant structural disorder associated to interstitial iodine in $MAPbI_3$ films.[40] This amphoteric defect can trap both electrons and holes through the +/0 and 0/- ionization levels placed at 0.57 and 0.29 eV below and above the CB and VB edges, respectively, as shown in Figure 1b, in agreement with previous results.[20] Confirming the picture discussed above, the boundary orbitals of V_I^0 and V_{Pb}^- only show shallow charge trapping, being delocalized CB and VB states typical of non-defective $MAPbI_3$ with some polarization around the defect sites, Figures 1c and 1e. For I_i^0 a localized unoccupied state is instead found within the material band gap, as shown in Figure 1d. The match between the calculated I_i density and the measured trap density in single crystals points at interstitial iodine as the source of traps experimentally observed.[12] Clearly, a distinction should be made between the most abundant defects (e.g. MA_i^+) and charge traps.

The neutral state of I_i^0 is notably not thermodynamically stable in the explored Fermi energy range so we expect this charge state to be metastable and only formed upon photoexcitation.[38, 39] The +/- transition of I_i is close to the native Fermi level, so one would in principle expect a relevant trapping activity. The two-electron nature of this transition, however, effectively inactivates this phenomenon. This is a typical behavior of the iodide (I_i^-) /tri-iodide (I_i^+) redox couple associated with retarded charge recombination in dye-sensitized solar cells.[41]

The calculated structures of I_i^+, I_i^0 and I_i^- are reported in Figures 2a-c. I_i^+ shows a trimer structure,[20,42] corresponding to one central I^+ bound on two sides by I^-, essentially the structure of a coordinated I_3^- molecule; I_i^- is instead the result of two symmetric I^- ions binding in a bridging coordination to two vicinal lead atoms. The most stable structure of I_i^0, hereafter I_i^0(a), is similar to that of I_i^- but shows an asymmetric bridging coordination with two comparable Pb-I bonds on one side and two elongated and asymmetric Pb-I bonds to the second lead atom. A secondary minimum,

I_i^0(b), corresponding to the in-plane analogue of I_i^0(a) was found by ab initio molecular dynamics simulations, shown in Supplementary Figure S4, and calculated to be 0.19 eV less stable than I_i^0(a), Figure 2d. The average calculated I-I distance in I_i^+ (2.95 Å) is typical of I_3^-; this parameter increases to 3.24 Å in I_i^0(a), typical of I_2^-; and in I_i^- it corresponds to two independently coordinated iodide ions, as shown in Figures 2a-c. Based on this analysis it is clear that charge trapping in $MAPbI_3$ is essentially associated to iodine redox chemistry.

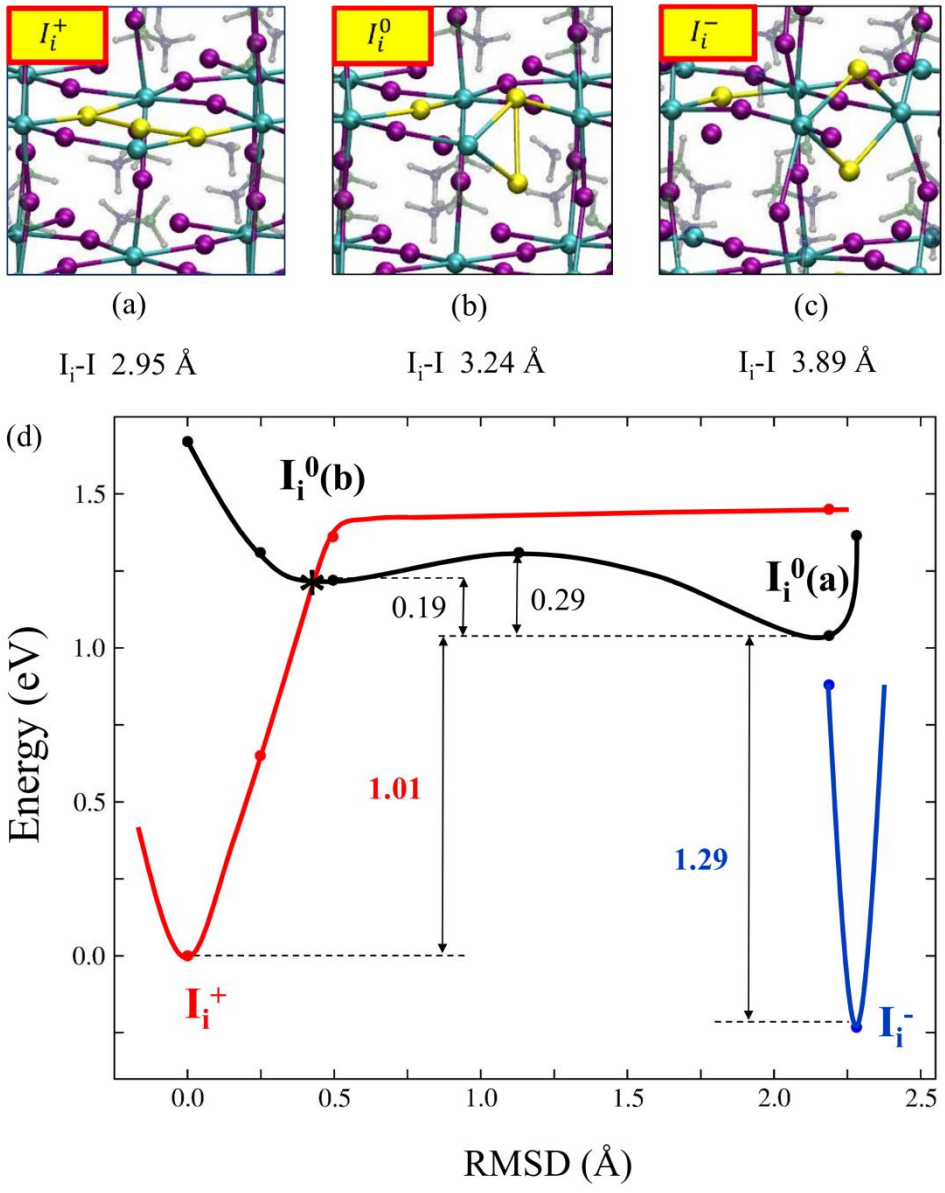

Figure 2.a-c) Local geometrical structures of interstitial iodine in its positive (a), more stable neutral (b) and negative(c) charge states, with associated I-I distances. Relevant iodine atoms involved in the trapping/detrapping processes are highlighted in yellow. For I_i^+ the average of the two I-I bond lengths in reported. d) Configuration diagrams (energy versus structural coordinates) of interstitial iodine in its positive (red), neutral (black) and negative (blue) charge states versus the root mean square displacement (RMSD) of the highlighted iodine atoms with respect to their position in I_i^+. The energies for the positive species are referenced to the VB maximum, while those of the negative species are referred to the CB minimum, simulating the energetics after photoexcitation (before recombination). The separate positive/neutral and negative/neutral energies have the same reference, thus they can be compared, while the positive/negative energies cannot be directly compared. The dots are calculated points while the solid lines are an interpolation of calculated points to guide to the eye.

Having characterized the minimum energy structures corresponding to each charge state of interstitial iodine, we are now in a position to draw a global configuration diagram of the trapping and recombination processes in $MAPbI_3$. This is shown in Figure 2d, where we report the calculated system's energy in its various charge states against a representative structural parameter, defined as the root mean square displacement (RMSD) of the reactive iodine atoms with respect to their position in I_i^+ (highlighted in yellow in Figure 2a-c). Trapping of an electron close to the I_i^+ minimum will drive the system towards the secondary I_i^0(b) minimum, which is the kinetically stable trapping product, shown in Supplementary Figure S4. To reach the I_i^0(a) global minimum of the neutral charge state the system needs to overcome a 0.10 eV energy barrier, see Figure 2d, gaining 0.19 eV. To recombine with a hole (or to release the trapped electron) and reform I_i^+, the system needs thus to overcome a barrier of 0.29 eV, I_i^0(a) $\rightarrow I_i^0$(b) pathway on the neutral curve in Figure 2d, since the positive curve is too high in energy (by 0.43 eV) when the system is close to I_i^0(a) and still fairly high (0.14 eV above) in I_i^0(b). Most likely, electron detrapping will thus occur

through a non-radiative recombination channel, due to the instability of I_i^+ up to the crossing point between the neutral and positive curves, denoted with a black * in Figure 2d. The energetically favorable electron trapping featuring a small barrier and the energetically disfavored detrapping process are fully consistent with the measurement of a recombination time of trapped electrons of several μs, more than one order of magnitude longer than their trapping rate.[14] Importantly, such rates could be probed only through photo-current and transient absorption measurements as a consequence of the non-radiative decay associated to the trapped electrons.[14]

In contrast to electron trapping, hole trapping at I_i^- is calculated to proceed with a small geometrical rearrangement, $I_i^- \rightarrow I_i^0(a)$ pathway in Figure 2d, with no barriers occurring on either the negative or neutral curve. As such, hole trapping is expected to be relatively fast, as is the related detrapping process, possibly contributing an efficient deactivation channel for photogenerated charge carriers. Li *et al.* have recently reported ab initio time-domain dynamics simulations showing faster hole than electron trapping on interstitial iodine,[43] consistent with our model.

Based on the almost coincident minimum of the neutral and negative curves, one may predict that radiative recombination, mediated by the overlap of vibrational functions of the two charge states, could in this case compete with non-radiative deactivation. In such a case, we predict a minimum to minimum $I_i^0(a) \rightarrow I_i^-$ radiative emission energy of 1.29 eV, thus falling in the near-IR. Notice that the different slope of the two charge states corresponding to the emission process may lead to a significant broadening of the emitted energy, since a small fluctuation around the shallow $I_i^0(a)$ minimum would imply a fairly large energy variation on steep I_i^- curve, Figure 2d.

To investigate how the proposed defect energetics would change when moving from the bulk to the surface, we have recalculated the DFEs of neutral defects (the only ones which can be trustfully calculated on surfaces) for the PbI_2-terminated surface of $MAPbI_3$, which is among the stable surface terminations of the perovskite.[44] The results, collected in Table S6, Supplementary Information, show, as expected, lower DFEs compared to the bulk, with more than 1 eV stabilization found in the case of iodine interstitials. Our results are in agreement with the work of

Uratani et al.,[45] who carried out a comprehensive study of the defects formation energies on different surface terminations. On overall, the defect chemistry in the bulk and on the surface of $MAPbI_3$ is qualitatively similar, with the surface inducing a higher density of defects by virtue of the lower DFE.

To verify the predictions of our theoretical model, we show in Figure 3a the steady state room-temperature photoluminescence (PL) spectrum of a typical $MAPbI_3$ polycrystalline thin film used in solar cell fabrication[46] collected over a spectral range between 1.65 and 1.0 eV, at a range of excitation densities, under nitrogen atmosphere. Together with the band-to-band radiative emission peaking close to 1.6 eV we find a weak, broad emission band spanning the 1.35-1.15 eV energy range. This emission is consistent with the predicted energetics for radiative recombination of trapped holes, Figure 2d, and is quenched as the excitation energy increases, a typical behaviour expected from radiative trap-assisted recombination. Increasing the excitation intensity fills the traps with photogenerated charge carriers, thus inactivating the traps unless a detrapping event occurs. Notably, such emissive states have been found to be populated and depopulated in a time window shorter than 1ns (see Supplementary Figure S5 and refs [47, 48]) indicative of an effective loss channel in solar cells. Notably, Tress e*t al.* have very recently reported a sub gap feature at 1.35 eV in perovskite solar cells, possibly linked to reduction of solar cell open circuit voltage below the radiative limit,[49] consistent with our spectroscopic observations and theoretical model.

In Figure 3b we show the photophysics of a second sample, for which the PL dynamics probed at 1.59 eV are compared with the transient-absorption dynamics probed at the photo-bleaching band found at 1.61 eV. The dynamics are recorded in a wide time range, from~1 ns to~1 ms. Briefly, the transient absorption spectrum represents the change in the absorbance, typically measured as a change in transmittance, of a probe white-light pulse through the sample induced by a photo-exciting pulse. The photo-excitation leads to the transfer of electrons from the VB to the CB leaving behind the holes. Due to the state-filling close to the band edges by the photo-excited species, and the resultant Pauli blocking, the absorption probability is reduced at the

associated photon energies.[4] This induces a transparency at the energy corresponding to the band-edge of the excited sample, measured as a positive ΔT/T (normalized transmittance change) signal (commonly referred to as a photo-bleach). The latter is proportional to the density of electrons and holes in the VB and CB respectively, and its dynamics will therefore follow the dynamics of free carriers, Supplementary Figure S6.

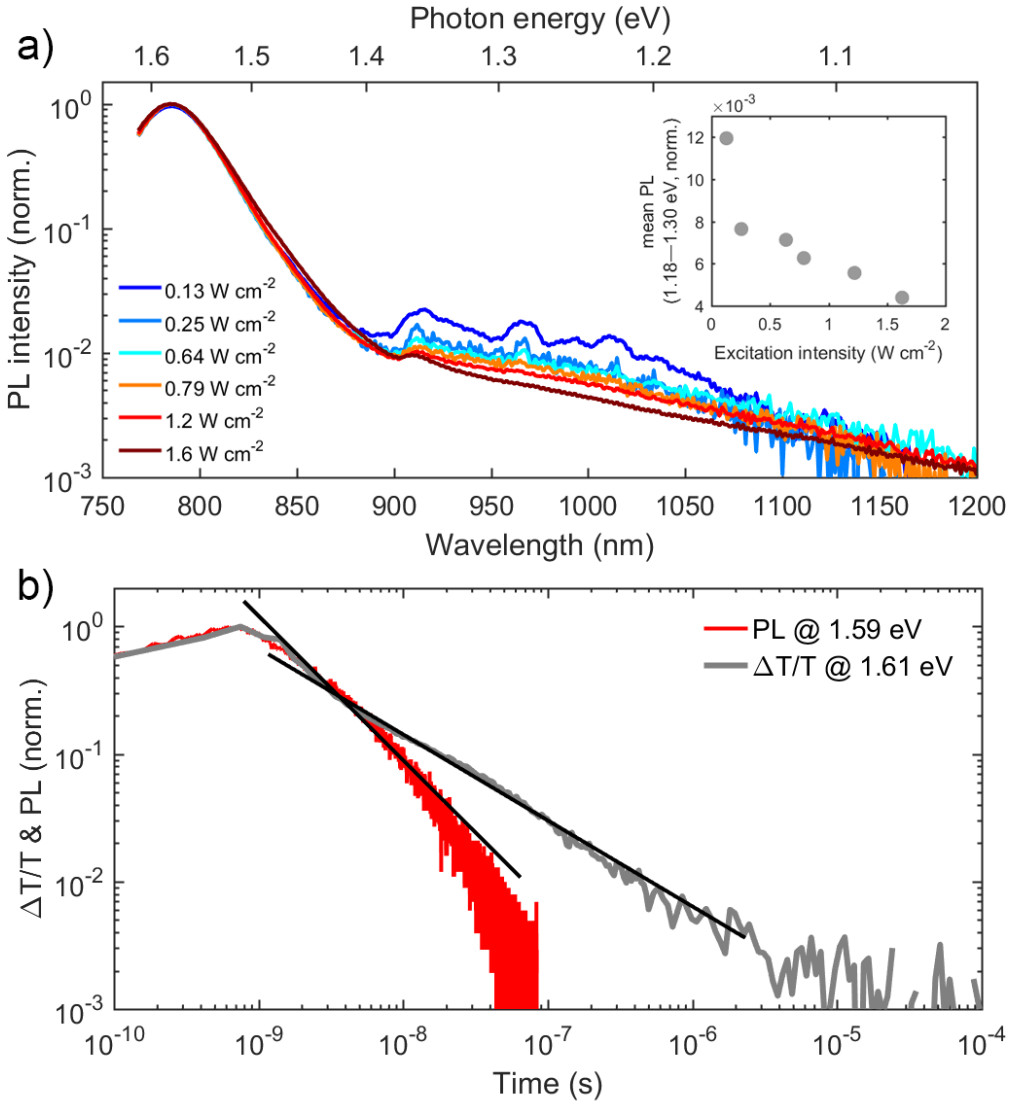

Figure 3. a) Steady state PL spectrum of $MAPbI_3$ as a function of excitation intensity (inset) at room temperature. b) PL dynamics probed at 1.59 eV (red trace) corresponding to the PL emission maximum and the dynamics probed at the photo-bleach band at 1.61 eV (grey) of the transient absorption spectrum. The straight lines are used as guide to the eye to highlight two different slopes in the log-log scale.

Figure 3b shows that the photo-bleach dynamics has two components, a short living one which almost perfectly matches the band gap PL dynamics up to ~6 ns (crossing of the black lines in Figure 3b) and a very long decay of tens of microseconds, which has no emissive analogue, thus corresponding to a non radiative decay process. Importantly, the population of the long living species increases as the sample temperature grows (see Supplementary Figure S7) suggesting the presence of an energy barrier to its formation. Based on the diagram presented in Figure 2, we assign the short living sub gap emissive band to the recombination of holes trapped by negative interstitial iodine with free electrons in the CB; and the slow component to non-radiative recombination of electrons trapped by positive interstitial iodine with free holes in the VB. In this latter case, we associate the experimentally observed thermally activated process to the trapping of electrons at I_i^+ and the subsequent relaxation to the global I_i^0(a) minimum, Figure 2d.

Notably, exciting $MAPbI_3$ under inert conditions can induce the formation of traps, which together with traps related to native defects may be passivated when the film is exposed to oxygen (see Supplementary Figure S8).[50, 51] This is consistent with the oxidation of I_i^- to I_i^+ (i.e. of iodide to tri-iodide) and with the consequent partial inactivation of hole traps, allowing us to clearly recognize the photophysical signature of trapped holes predicted by calculations. Under mild oxidizing conditions, likely met during conventional solution perovskite synthesis,[52] *hole traps can be converted to kinetically inactive electron traps*, explaining the apparent defect tolerance of metal-halide perovskites.

Based on the same model, we are also able to propose a possible role for bromine and chlorine doping of $MAPbI_3$. We report in Figure 4 the optimized structures of Br- and Cl-doped $MAPbI_3$ in the presence of I_i^-. We considered two different positions of the hetero-halide, i.e. substituting an interstitial iodine (shown in Figures 4a-c) or substituting a lattice iodine atom (Supplementary Figure S9). For both bromine and chlorine doping, substitution of an interstitial iodine is favored by ~0.1 eV compared to leaving an intact interstitial iodine and substituting a

lattice iodine. Despite the fairly low energy difference, a clear propensity for smaller halides to occupy interstitial positions is predicted, in line with the expectations based on the decreased ionic radius. Most notably, the defect transition levels associated to interstitial bromine and chlorine doping are displaced in energy by ~0.3 eV towards the VB, Figure 4d, transforming such mixed-halide interstitials into shallow traps. The introduction of hetero-halides in $MAPbI_3$ may thus constitute a possible mechanism of inactivation of hole traps. The downshift of the 0/- transition upon interstitial halide doping, again related to the typical halide redox chemistry, is fully consistent with the reported enhanced photovoltaic performance[53] and carrier lifetime[54] in bromine-doped $MAPbI_3$ perovskite solar cells and with the established beneficial effect of chlorine doping in $MAPbI_3$.[15] Notably, while a different morphology is usually obtained for Cl-doped samples originated by $PbCl_2$ due to the slowing down of the film formation,[55] the proposed "curing" effect extends beyond the change expected for the marginally different sample morphology of pure and bromine-doped perovskites, see SEM micrographs in Supplementary Figure S10 and Ref.[54].

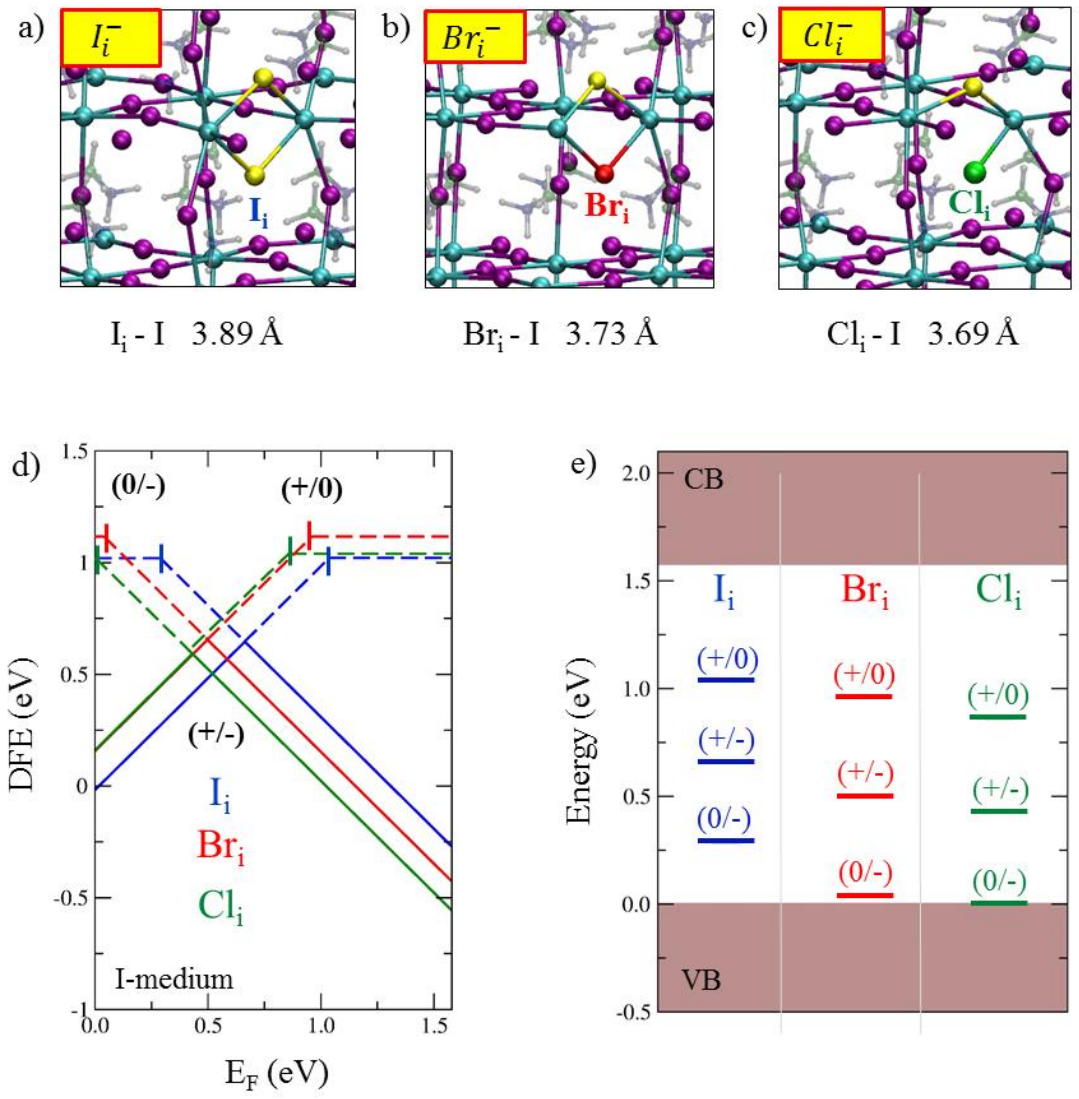

Figure 4.a-c) Local geometrical structures of interstitial iodine in its negative charge states. a) Native I_i^-; b) bromine-substituted I_i^-; c) chlorine-substituted I_i^-. d) Defect formation energy (DFE, eV) diagram versus the Fermi energy (E_F, eV) for halide interstitials in $MAPbI_3$. Solid lines indicate the stable charge states of a given defect, while the blue lines indicate the metastable neutral state of I_i. Blue, red and green lines refer to native I_i^-, bromine-substituted and chlorine-substituted I_i^-, respectively. e) Thermodynamic transition levels for the native I_i^-, bromine-substituted and chlorine-substituted I_i^- (blue, red and green lines, respectively).

Confirming the healing effect of bromine doping, we have prepared a $MAPbI_3$ sample containing 5% excess MABr and probed the PL decay of such sample, see Supplementary Figure S11. A

substantially longer PL lifetime is observed for the Br-doped sample, consistent with the proposed curing of deep traps. Furthermore, we carried out TA experiments on the same sample, see Figure S12 in Supplementary Information. One can notice an elongation of the initial decay lifetime of the Br-doped sample against the pure $MAPbI_3$, while the dynamics of the long tail assigned to the electron lifetime does not seem to change. No distinguishable signature of sub-band gap emission could be observed for this sample. Altogether, this data supports our suggestion that a slight bromine doping will mainly affect the detrimental hole trapping occurring on short time scales.

Concluding Remarks

In conclusion, we have rationalized the defect chemistry and related photo-physics which determine the so-called "defect tolerance" in metal-halide perovskites. We have identified intrinsic charge traps and revealed that they are dominated by the peculiar iodine redox chemistry, which has been known and exploited for long time to retard charge recombination in dye-sensitized solar cells. We show that hole traps due to interstitial iodine are potentially detrimental deep traps, which can however be converted to long-lived, kinetically inactive electron traps by adjusting and possibly controlling the oxidizing conditions during and after the perovskite synthesis. Notably, iodide oxidation to tri-iodide is catalyzed by acids,[56] therefore the acidic methylammonium cation and water traces may well provide unintentional catalysts for such transformation. Importantly, this clarifies the controversial reports which can be found in literature on the large variety of thin films with different optoelectronic quality, in the presence of oxidizing agents.[57] In fact, while a strong oxidative environment will subtract iodide to the perovskite formation, possibly limiting the grain size and overall optoelectronic material quality,[52] post-synthesis exposure to mild oxidizing agents could transform harmful hole traps into kinetically inactive electron traps. Notably, devices prepared from a vacuum deposition process showed optimal efficiency for a slight under stoichiometric I:Pb ratio (~2.8:1),[58]consistent with the inhibition of interstitial iodine formation in such a slightly iodine-poor environment.

Based on the proposed model we have also identified how bromine and chlorine doping may constitute an additional means of hole traps curing. This is due to the stability of hetero-halide substitution of interstitial iodine which shifts the associated thermodynamic transition levels from deep to shallow due to the higher oxidation potential of bromide and chloride compared to iodide. The combination of various cations, including the less acidic formamidinium ion and of cesium, as well as of iodide and bromide, showing a different defect redox chemistry, in mixed perovskite formulations is likely at the heart of the superior photovoltaic efficiency and long-term stability of solar cells fabricated with these materials.[59]

Methods.

Computational details. All calculations have been performed on the tetragonal $MAPbI_3$, the stable phase at room temperature, adopting the experimental lattice parameters a=b=8.849 Å and c=12.642 Å.[60] The stabilities of native defects have been investigated by calculating the associated defects formation energies (DFE) by using a 2x2x1 supercell. In all cases, the most stable orientation of the methylammonium cations found for bulk $MAPbI_3$ [61] was initially set, followed by local structural relaxation. The DFEs have been calculated by using the equation (1) in the main text. All the simulations started with an isotropic MA cation orientation, which was approximately preserved in the optimized structures. Long-ranged electrostatic interactions between charged defects have been corrected following the approach of Freysoldt-Neugebauer-Van de Walle[62] by using gaussian model charges in a dielectric medium. In our approach both the electronic and ionic screenings due to the relaxation of the ions upon defect formation have been included in the model. To this aim, the ionic dielectric permittivity calculated at the PBE level (24) was used to correct the calculated DFT electrostatic potentials of charged defects within the supercell. The chemical potentials of the atomic species have been set in order to simulate three different chemical conditions, namely I-rich, I-medium and I-poor conditions, under the constraint of the thermodynamic stability of the $MAPbI_3$ phase. The chemical potentials of $MAPbI_3$ constituents, i.e. Pb, I and MA, in thermodynamic

equilibriums with the PbI_2 and MAI phases, have been evaluated by imposing the following relations among the chemical potentials

$$\mu(MA) + \mu(Pb) + 3\mu(I) = \Delta_f H(MAPbI_3) \quad (2)$$

$$\mu(MA) + \mu(I) < \Delta_f H(MAI) \quad (3)$$

$$\mu(Pb) + 2\mu(I) = \Delta_f H(PbI_2) \quad (4)$$

where the chemical potentials of the species I and Pb has been referenced to the value of the I_2 molecule and Pb bulk metal, respectively. The chemical potentials of the Br and Cl interstitials have been calculated by imposing the equilibrium with the $PbBr_2$ and $PbCl_2$ phases in the solubility limit, i.e. $\mu(Pb) + 2\mu(Br) = \Delta_f H(PbBr_2)$ and $\mu(Pb) + 2\mu(Cl) = \Delta_f H(PbCl_2)$.

The defects density of specie X_i in the state of charge q_i, C_{Xi} , at room temperature has been estimated by applying the Boltzmann equation $C_X = N_c exp(-DFE/k_BT)$, where N_c is the density of defects sites in the pristine material (10^{22} cm^{-3} for I, MA and $4x10^{21}$ cm^{-3} for Pb), *DFE* is the defect formation energy of specie X_i at the native Fermi level, k_B is the Boltzman constant and T the temperature (300K). The native Fermi level in each condition of growth at 300K has been calculated by solving the electro-neutrality equation for all the modelled defects, i.e. by finding the Fermi level such that $p - n + \sum_{Xi} q_i C_{Xi}(E_F) = 0$, where p and n are the intrinsic carriers densities of holes and electrons at room temperature The equilibrium structures of the defects have been calculated by using the Perdew-Burke-Ernzerhof (PBE) exchange-correlation functional,[63] relaxing the ion positions until forces on atoms was less than 0.001 Ryd/Å. PBE calculations have been performed using ultrasoft pseudopotentials (US) and plane waves basis sets. A cutoff on the plane waves of 40 Ryd and on the charge grid of 320 Ryd has been used, sampling the Brillouin Zone (BZ) with a Gamma centered 1x1x2 Monkhorst-Pack (MP) grid of k points.[64]

The equilibrium structures of the defects have been used to calculate the DFEs at the HSE06-SOC [65] level of theory. To be consistent with previous results in the literature,[20] the fraction of exact exchange has been set to 0.43. A comparison between various calculated quantities with such

modified functional and the standard HSE06 functional can be found in Table S5. Norm conserving (NC) pseudopotentials have been employed with a cutoff of 40 Ryd on the PWs and 1x1x2 MP grids of k points in the BZ, in order to reduce the computational efforts. Benchmark calculations at 70 Ryd with NC pseudopotentials have been performed to check the accuracy of the approach, see discussion in Supplementary Information. To quantitatively estimate the DFEs we included dispersion corrections, as implemented in the DFT-D3 scheme of Grimme,[66] to the energies calculated by HSE06-SOC. All calculations have been carried out with the QuantumEspresso simulation package.[67]

Sample preparation. N,N-dimethylformamide (DMF, anhydrous, 99.8%), and lead (II) acetate trihydrate (PbAc, 99.999%, CAS no. 6080-56-4) were purchased from Sigma-Aldrich; Methylammonium iodide (MAI, CAS no. 14965-49-2) and methylammonium bromide (MABr, CAS no.) were purchased from Dyesol. All chemicals were used without any further purification. Glass substrates were cleaned sequentially in Hellmanex (1 vol% in deionized water), deionized water, isopropyl alcohol (IPA), acetone and IPA again for 10 minutes each by sonication. The cleaned glass substrates were treated with Oxygen plasma for 10 minutes immediately prior to film deposition. Thin films were prepared in a nitrogen filled glovebox following a similar procedure to Zhang et al.[68] Precursor solutions of $Pb(Ac)_2$:MAI:MABr in a molar ratio of 1:3:0 or 1:3:0.15 were prepared in DMF with a concentration of ~30 wt%. Thin films were prepared by spin coating onto glass substrates at 2000 rpm, with an acceleration of 2000 rpm/s, for 45 s. The films were initially dried at room temperature for 15 minutes and then annealed at 100°C for 5 minutes. The thin film measured in Figure 3a was prepared as described in ref.[46]

Steady-state PL. The excitation source was a diode laser (400 nm cw). The thin film samples were mounted in a nitrogen-filled integrating sphere, and PL was and focused into a spectrograph (Andor Shamrock) coupled to an InGaAs photodiode array (Andor iDus).

Time-resolved Photoluminescence. The thin film samples were mounted in a chamber in vacuum (under 10^{-5} mbar) that was vented with room atmosphere for comparison of dynamics. PL was collected in reflection geometry, perpendicular to the excitation line. Samples were excited from both sides of the sample (glass substrate or sample film), without any relevant difference between them.Time-resolved PL measurements on $MAPbI_3$ films were performed using a Time Correlated Single Photon Counting setup. The output of an unamplified tunable Ti:Sapphire laser (Coherent Chameleon Ultra II, temporal and spectral bandwidths of ~140 fs and ~5 nm, respectively) was tuned for central wavelengths of 700 nm and then directed to the sample. The measurements were performed with excitation at 4 MHz, obtained using an acousto-optical modulating pulse picker (APE Pulse Select). The PL was collected and focused onto a spectrometer coupled to a N_2 cooled photomultiplier.

Transient Absorption Spectroscopy. Thin film samples were mounted in a chamber in vacuum (under 10^{-5} mbar). Transient absorption signal was collected in transmission geometry.An amplified Ti:sapphire laser (Quantronix Integra-C) generates ~100 fs pulses centered at 800 nm, running at 1 kHz. A broadband white light probe is generated by focusing the pulses into a thin sapphire plate. 532 nm pump light is obtained from a Q-switched $Nd:YVO_4$ laser (Innolas Picolo) which is electronically triggered and synchronized to the Ti:sapphire laser via an electronic delay. The pump pulses have a width of ~700 ps FWHM. Including jitter, the system has an instrument response function FWHM <1 ns. After interaction with the sample, a homebuilt prism spectrometer disperses the probe light on to a fast CCD array, enabling broadband shot-to-shot detection.

References

1. Green, M. A.; Ho-Baillie, A.; Snaith, H. J. The emergence of perovskite solar cells. *Nat. Photon.* **2014**, 8, 506-514.
2. Miyata, A.; Mitioglu, A.; Plochocka, P.; Portugall, O.; Wang, J. T.-W.; Stranks, S. D.; Snaith, H. J.; Nicholas, R. J. Direct measurement of the exciton binding energy and effective masses for charge carriers in organic-inorganic tri-halide perovskites. *Nat. Phys.* **2015**, 11, 582-587.
3. Lin, Q.; Armin, A.; Nagiri, R. C. R.; Burn, P. L.; Meredith, P. Electro-optics of perovskite solar cells. *Nat. Photon.* **2015**, 9, 106-112.

4. Srimath Kandada, A. R.; Petrozza, A. Photophysics of Hybrid Lead Halide Perovskites: The Role of Microstructure. *Acc. Chem. Res.* **2016**, 49, 536-544.
5. Wehrenfennig, C.; Eperon, G. E.; Johnston, M. B.; Snaith, H. J.; Herz, L. M. High Charge Carrier Mobilities and Lifetimes in Organolead Trihalide Perovskites. *Adv. Mater.* **2014**, 26, 1584-1589.
6. Stranks, S. D.; Eperon, G. E.; Grancini, G.; Menelaou, C.; Alcocer, M. J. P.; Leijtens, T.; Herz, L. M.; Petrozza, A.; Snaith, H. J. Electron-Hole Diffusion Lengths Exceeding 1 Micrometer in an Organometal Trihalide Perovskite Absorber. *Science* **2013**, 342, 341-344.
7. Jeon, N. J.; Noh, J. H.; Yang, W. S.; Kim, Y. C.; Ryu, S.; Seo, J.; Seok, S. I. Compositional engineering of perovskite materials for high-performance solar cells. *Nature* **2015**, 517, 476-480.
8. Zhou, H.; Chen, Q.; Li, G.; Luo, S.; Song, T.-b.; Duan, H.-S.; Hong, Z.; You, J.; Liu, Y.; Yang, Y. Interface engineering of highly efficient perovskite solar cells. *Science* **2014**, 345, 542-546.
9. Zhu, H.; Miyata, K.; Fu, Y.; Wang, J.; Joshi, P. P.; Niesner, D.; Williams, K. W.; Jin, S.; Zhu, X.-Y. Screening in crystalline liquids protects energetic carriers in hybrid perovskites. *Science* **2016**, 353, 1409-1413.
10. Miyata, K.; Meggiolaro, D.; Trinh, M. T.; Joshi, P. P.; Mosconi, E.; Jones, S. C.; De Angelis, F.; Zhu, X.-Y. Large polarons in lead halide perovskites. *Sci. Adv.* **2017**, 3.
11. Neukirch, A. J.; Nie, W.; Blancon, J.-C.; Appavoo, K.; Tsai, H.; Sfeir, M. Y.; Katan, C.; Pedesseau, L.; Even, J.; Crochet, J. J.; Gupta, G.; Mohite, A. D.; Tretiak, S. Polaron Stabilization by Cooperative Lattice Distortion and Cation Rotations in Hybrid Perovskite Materials. *Nano Lett.* **2016**, 16, 3809-3816.
12. Adinolfi, V.; Yuan, M.; Comin, R.; Thibau, E. S.; Shi, D.; Saidaminov, M. I.; Kanjanaboos, P.; Kopilovic, D.; Hoogland, S.; Lu, Z.-H.; Bakr, O. M.; Sargent, E. H. The In-Gap Electronic State Spectrum of Methylammonium Lead Iodide Single-Crystal Perovskites. *Adv. Mater.* **2016**, DOI: 10.1002/adma.201505162.
13. Chen, Y.; Yi, H. T.; Wu, X.; Haroldson, R.; Gartstein, Y. N.; Rodionov, Y. I.; Tikhonov, K. S.; Zakhidov, A.; Zhu, X. Y.; Podzorov, V. Extended carrier lifetimes and diffusion in hybrid perovskites revealed by Hall effect and photoconductivity measurements. *Nat. Commun.* **2016**, 7, 12253.
14. Leijtens, T.; Eperon, G. E.; Barker, A. J.; Grancini, G.; Zhang, W.; Ball, J. M.; Kandada, A. R. S.; Snaith, H. J.; Petrozza, A. Carrier trapping and recombination: the role of defect physics in enhancing the open circuit voltage of metal halide perovskite solar cells. *Energy Environ. Sci.* **2016**, 9, 3472-3481.
15. deQuilettes, D. W.; Vorpahl, S. M.; Stranks, S. D.; Nagaoka, H.; Eperon, G. E.; Ziffer, M. E.; Snaith, H. J.; Ginger, D. S. Impact of microstructure on local carrier lifetime in perovskite solar cells. *Science* **2015**, 348, 683-686.
16. Yin, W.-J.; Shi, T.; Yan, Y. Unusual defect physics in CH3NH3PbI3 perovskite solar cell absorber. *Appl. Phys. Lett.* **2014**, 104, 063903.
17. Buin, A.; Comin, R.; Xu, J.; Ip, A. H.; Sargent, E. H. Halide-Dependent Electronic Structure of Organolead Perovskite Materials. *Chem. Mater.* **2015**, 27, 4405-4412.
18. Agiorgousis, M. L.; Sun, Y.-Y.; Zeng, H.; Zhang, S. Strong Covalency-Induced Recombination Centers in Perovskite Solar Cell Material CH3NH3PbI3. *J. Am. Chem. Soc.* **2014**, 136, 14570-14575.
19. Walsh, A.; Scanlon, D. O.; Chen, S.; Gong, X. G.; Wei, S.-H. Self-Regulation Mechanism for Charged Point Defects in Hybrid Halide Perovskites. *Angew. Chem. Int. Ed.* **2014**, 53, 1-5.
20. Du, M.-H. Density Functional Calculations of Native Defects in CH3NH3PbI3: Effects of Spin–Orbit Coupling and Self-Interaction Error. *J. Phys. Chem. Lett.* **2015**, 6, 1461-1466.
21. Shockley, W.; Read, W. T. Statistics of the Recombinations of Holes and Electrons. *Phys. Rev.* **1952**, 87, 835-842.
22. Ueki, T.; Itsumi, M.; Takeda, T. Octahedral void defects observed in the bulk of Czochralski silicon. *Appl. Phys. Lett.* **1997**, 70, 1248-1250.

23. Ayres, J. R. Characterization of trapping states in polycrystalline-silicon thin film transistors by deep level transient spectroscopy. *J. Appl. Phys.* **1993**, 74, 1787-1792.
24. Balcioglu, A.; Ahrenkiel, R. K.; Hasoon, F. Deep-level impurities in CdTe/CdS thin-film solar cells. *J. Appl. Phys.* **2000**, 88, 7175-7178.
25. Kerr, L. L.; Li, S. S.; Johnston, S. W.; Anderson, T. J.; Crisalle, O. D.; Kim, W. K.; Abushama, J.; Noufi, R. N. Investigation of defect properties in Cu(In,Ga)Se2 solar cells by deep-level transient spectroscopy. *Solid-State Electronics* **2004**, 48, 1579-1586.
26. Blancon, J.-C.; Nie, W.; Neukirch, A. J.; Gupta, G.; Tretiak, S.; Cognet, L.; Mohite, A. D.; Crochet, J. J. The Effects of Electronic Impurities and Electron–Hole Recombination Dynamics on Large-Grain Organic–Inorganic Perovskite Photovoltaic Efficiencies. *Adv. Funct. Mater.* **2016**, 26, 4283-4292.
27. Zhang, W.; Saliba, M.; Moore, D. T.; Pathak, S. K.; Hörantner, M. T.; Stergiopoulos, T.; Stranks, S. D.; Eperon, G. E.; Alexander-Webber, J. A.; Abate, A.; Sadhanala, A.; Yao, S.; Chen, Y.; Friend, R. H.; Estroff, L. A.; Wiesner, U.; Snaith, H. J. Ultrasmooth organic–inorganic perovskite thin-film formation and crystallization for efficient planar heterojunction solar cells. *Nat. Commun.* **2015**, 6, 6142.
28. Yin, W.-J.; Shi, T.; Yan, Y. Unique Properties of Halide Perovskites as Possible Origins of the Superior Solar Cell Performance. *Adv. Mater.* **2014**, 26, 4653-4658.
29. Umari, P.; Mosconi, E.; De Angelis, F. Relativistic GW calculations on $CH_3NH_3PbI_3$ and $CH_3NH_3SnI_3$ Perovskites for Solar Cell Applications. *Sci. Rep.* **2014**, 4, 4467.
30. Alkauskas, A.; Pasquarello, A. Band-edge problem in the theoretical determination of defect energy levels: The O vacancy in ZnO as a benchmark case. *Phys. Rev. B* **2011**, 84, 125206.
31. Iwata, J.-I. S., Keisuke; Oshiyama, Atsushi A precaution for the hybrid density functional calculation of open-shell systems. **2016**, arXiv:1605.00338.
32. Shi, D.; Adinolfi, V.; Comin, R.; Yuan, M.; Alarousu, E.; Buin, A.; Chen, Y.; Hoogland, S.; Rothenberger, A.; Katsiev, K.; Losovyj, Y.; Zhang, X.; Dowben, P. A.; Mohammed, O. F.; Sargent, E. H.; Bakr, O. M. Low trap-state density and long carrier diffusion in organolead trihalide perovskite single crystals. *Science* **2015**, 347, 519-522.
33. Sadoughi, G.; Starr, D. E.; Handick, E.; Stranks, S. D.; Gorgoi, M.; Wilks, R. G.; Bär, M.; Snaith, H. J. Observation and Mediation of the Presence of Metallic Lead in Organic–Inorganic Perovskite Films. *ACS Appl. Mater. Interfaces* **2015**, 7, 13440-13444.
34. Azpiroz, J. M.; Mosconi, E.; Bisquert, J.; De Angelis, F. Defect migration in methylammonium lead iodide and its role in perovskite solar cell operation. *Energy Environ. Sci.* **2015**, 8, 2118-2127.
35. Ming, W.; Chen, S.; Du, M.-H. Chemical instability leads to unusual chemical-potential-independent defect formation and diffusion in perovskite solar cell material CH3NH3PbI3. *J. Mater. Chem. A* **2016**, 4, 16975-16981.
36. Yang, J.-H.; Yin, W.-J.; Park, J.-S.; Wei, S.-H. Fast self-diffusion of ions in CH3NH3PbI3: the interstiticaly mechanism versus vacancy-assisted mechanism. *J. Mater. Chem. A* **2016**, 4, 13105-13112.
37. Eames, C.; Frost, J. M.; Barnes, P. R. F.; O'Regan, B. C.; Walsh, A.; Islam, M. S. Ionic transport in hybrid lead iodide perovskite solar cells. *Nat. Commun.* **2015**, 6, 7497.
38. Mosconi, E.; Meggiolaro, D.; Snaith, H. J.; Stranks, S. D.; De Angelis, F. Light-induced annihilation of Frenkel defects in organo-lead halide perovskites. *Energy Environ. Sci.* **2016**, 9, 3180-3187.
39. Mosconi, E.; De Angelis, F. Mobile Ions in Organohalide Perovskites: Interplay of Electronic Structure and Dynamics. *ACS Energy Lett.* **2016**, 1, 182-188.
40. Minns, J. L.; Zajdel, P.; Chernyshov, D.; van Beek, W.; Green, M. A. Structure and interstitial iodide migration in hybrid perovskite methylammonium lead iodide. *Nat. Commun.* **2017**, 8, 15152.
41. Boschloo, G.; Hagfeldt, A. Characteristics of the Iodide/Triiodide Redox Mediator in Dye-Sensitized Solar Cells. *Acc. Chem. Res.* **2009**, 42, 1819-1826.

42. Du, M. H. Efficient carrier transport in halide perovskites: theoretical perspectives. *J. Mater. Chem. A* **2014**, 2, 9091-9098.
43. Li, W.; Liu, J.; Bai, F.-Q.; Zhang, H.-X.; Prezhdo, O. V. Hole Trapping by Iodine Interstitial Defects Decreases Free Carrier Losses in Perovskite Solar Cells: A Time-Domain Ab Initio Study. *ACS Energy Lett.* **2017**, 2, 1270-1278.
44. Haruyama, J.; Sodeyama, K.; Han, L.; Tateyama, Y. Termination Dependence of Tetragonal CH3NH3PbI3 Surfaces for Perovskite Solar Cells. *J. Phys. Chem. Lett.* **2014**, 5, 2903-2909.
45. Uratani, H.; Yamashita, K. Charge Carrier Trapping at Surface Defects of Perovskite Solar Cell Absorbers: A First-Principles Study. *J. Phys. Chem. Lett.* **2017**, 8, 742-746.
46. Deschler, F.; Price, M.; Pathak, S.; Klintberg, L. E.; Jarausch, D.-D.; Higler, R.; Hüttner, S.; Leijtens, T.; Stranks, S. D.; Snaith, H. J.; Atatüre, M.; Phillips, R. T.; Friend, R. H. High Photoluminescence Efficiency and Optically Pumped Lasing in Solution-Processed Mixed Halide Perovskite Semiconductors. *J. Phys. Chem. Lett.* **2014**, 5, 1421-1426.
47. Wehrenfennig, C.; Liu, M.; Snaith, H. J.; Johnston, M. B.; Herz, L. M. Charge carrier recombination channels in the low-temperature phase of organic-inorganic lead halide perovskite thin films. *APL Materials* **2014**, 2, 081513.
48. Wu, X.; Trinh, M. T.; Niesner, D.; Zhu, H.; Norman, Z.; Owen, J. S.; Yaffe, O.; Kudisch, B. J.; Zhu, X. Y. Trap States in Lead Iodide Perovskites. *J. Am. Chem. Soc.* **2015**, 137, 2089-2096.
49. Tress, W.; Yavari, M.; Domanski, K.; Yadav, P.; Niesen, B.; Correa Baena, J. P.; Hagfeldt, A.; Graetzel, M. Interpretation and evolution of open-circuit voltage, recombination, ideality factor and subgap defect states during reversible light-soaking and irreversible degradation of perovskite solar cells. *Energy Environ. Sci.* **2018**.
50. Motti, S. G.; Gandini, M.; Barker, A. J.; Ball, J. M.; Srimath Kandada, A. R.; Petrozza, A. Photoinduced Emissive Trap States in Lead Halide Perovskite Semiconductors. *ACS Energy Lett.* **2016**, 1, 726-730.
51. Meggiolaro, D.; Mosconi, E.; De Angelis, F. Mechanism of Reversible Trap Passivation by Molecular Oxygen in Lead-Halide Perovskites. *ACS Energy Lett.* **2017**, 2794-2798.
52. Zhang, W.; Pathak, S.; Sakai, N.; Stergiopoulos, T.; Nayak, P. K.; Noel, N. K.; Haghighirad, A. A.; Burlakov, V. M.; deQuilettes, D. W.; Sadhanala, A.; Li, W.; Wang, L.; Ginger, D. S.; Friend, R. H.; Snaith, H. J. Enhanced optoelectronic quality of perovskite thin films with hypophosphorous acid for planar heterojunction solar cells. *Nat. Commun.* **2015**, 6, 10030.
53. Noh, J. H.; Im, S. H.; Heo, J. H.; Mandal, T. N.; Seok, S. I. Chemical Management for Colorful, Efficient, and Stable Inorganic−Organic Hybrid Nanostructured Solar Cells. *Nano Lett.* **2013**, 13, 1764-1769.
54. Kiermasch, D.; Rieder, P.; Tvingstedt, K.; Baumann, A.; Dyakonov, V. Improved charge carrier lifetime in planar perovskite solar cells by bromine doping. *Sci. Rep.* **2016**, 6, 39333.
55. Williams, S. T.; Zuo, F.; Chueh, C.-C.; Liao, C.-Y.; Liang, P.-W.; Jen, A. K. Y. Role of Chloride in the Morphological Evolution of Organo-Lead Halide Perovskite Thin Films. *ACS Nano* **2014**, 8, 10640-10654.
56. Ayscough, P. B.; Burchill, C. E.; Ivin, K. J.; Logan, S. R. The photochemical oxidation of aqueous iodide solutions: An experiment demonstrating the competitive reactions of the hydrated electron. *J. Chem. Educ.* **1967**, 44, 349.
57. Eperon, G. E.; Habisreutinger, S. N.; Leijtens, T.; Bruijnaers, B. J.; van Franeker, J. J.; deQuilettes, D. W.; Pathak, S.; Sutton, R. J.; Grancini, G.; Ginger, D. S.; Janssen, R. A. J.; Petrozza, A.; Snaith, H. J. The Importance of Moisture in Hybrid Lead Halide Perovskite Thin Film Fabrication. *ACS Nano* **2015**, 9, 9380-9393.
58. Kim, B.-S.; Choi, M.-H.; Choi, M.-S.; Kim, J.-J. Composition-controlled organometal halide perovskite via CH3NH3I pressure in a vacuum co-deposition process. *J. Mater. Chem. A* **2016**, 4, 5663-5668.
59. McMeekin, D. P.; Sadoughi, G.; Rehman, W.; Eperon, G. E.; Saliba, M.; Hörantner, M. T.; Haghighirad, A.; Sakai, N.; Korte, L.; Rech, B.; Johnston, M. B.; Herz, L. M.; Snaith, H. J. A

mixed-cation lead mixed-halide perovskite absorber for tandem solar cells. *Science* **2016**, 351, 151-155.
60. Stoumpos, C. C.; Malliakas, C. D.; Kanatzidis, M. G. Semiconducting Tin and Lead Iodide Perovskites with Organic Cations: Phase Transitions, High Mobilities, and Near-Infrared Photoluminescent Properties. *Inorg. Chem.* **2013**, 52, 9019-9038.
61. Quarti, C.; Mosconi, E.; De Angelis, F. Interplay of Orientational Order and Electronic Structure in Methylammonium Lead Iodide: Implications for Solar Cell Operation. *Chem. Mater.* **2014**, 26, 6557–6569.
62. Freysoldt, C.; Neugebauer, J.; Van de Walle, C. G. Fully Ab Initio Finite-Size Corrections for Charged-Defect Supercell Calculations. *Phys. Rev. Lett.* **2009**, 102, 016402.
63. Perdew, J. P.; Burke, K.; Ernzerhof, M. Generalized Gradient Approximation Made Simple. *Phys. Rev. Lett.* **1996**, 77, 3865-3868.
64. Monkhorst, H. J.; Pack, J. D. Special points for Brillouin-zone integrations. *Phys. Rev. B* **1976**, 13, 5188-5192.
65. Heyd, J.; Scuseria, G. E.; Ernzerhof, M. Hybrid functionals based on a screened Coulomb potential. *J. Chem. Phys.* **2003**, 118, 8207-8215.
66. Grimme, S.; Antony, J.; Ehrlich, S.; Krieg, H. A consistent and accurate ab initio parametrization of density functional dispersion correction (DFT-D) for the 94 elements H-Pu. *J. Chem. Phys.* **2010**, 132, 154104.
67. Giannozzi, P.; Baroni, S.; Bonini, N.; Calandra, M.; Car, R.; Cavazzoni, C.; Ceresoli, D.; Guido, L. C.; Cococcioni, M.; Dabo, I.; Corso, A. D.; Gironcoli, S. d.; Fabris, S.; Fratesi, G.; Gebauer, R.; Gerstmann, U.; Gougoussis, C.; Kokalj, A.; Lazzeri, M.; Martin-Samos, L.; Marzari, N.; Mauri, F.; Mazzarello, R.; Paolini, S.; Pasquarello, A.; Paulatto, L.; Sbraccia, C.; Scandolo, S.; Sclauzero, G.; Seitsonen, A. P.; Smogunov, A.; Umari, P.; Wentzcovitch, R. M. QUANTUM ESPRESSO: a modular and open-source software project for quantum simulations of materials. *J. Phys.: Condens. Matter* **2009**, 21, 395502.
68. Zhang, W.; Pathak, S.; Sakai, N.; Stergiopoulos, T.; Nayak, P. K.; Noel, N. K.; Haghighirad, A. A.; Burlakov, V. M.; deQuilettes, D. W.; Sadhanala, A.; Li, W.; Wang, L.; Ginger, D. S.; Friend, R. H.; Snaith, H. J. Enhanced optoelectronic quality of perovskite thin films with hypophosphorous acid for planar heterojunction solar cells. *Nat. Commun.* **2015**, 6, 10030.